CrossMark
click for updates

ZnO rods rooted on manifold carbon nanofiber paper as a scalable photocatalyst platform: the effects of ZnO morphology†

Sung-Ho Hwang,[a] Young Kwang Kim,[a] Song Hyun Yoon,[a] Sang Kyoo Lim*[a] and Hyunwoong Park*[b]

Crystalline ZnO rods rooted on manifold carbon nanofiber (CNF) paper were synthesized *via* electrodeposition of ZnO onto electrospun CNF paper (∼300 μm thick) followed by oxidative annealing. The morphology of the ZnO deposited on the conductive CNF paper can be tailored to be polycrystalline rods with convex-shaped ends at a high Zn^{2+} precursor concentration (0.5 mM) upon annealing (denoted CZ-a-0.5, where "a" refers to annealing), whereas the sample electrodeposited at a low Zn^{2+} precursor concentration (0.25 mM) results in single crystalline rods with concave-shaped ends (denoted CZ-a-0.25). In order to systematically examine the photocatalytic activity, the annealed and non-annealed CNF/ZnO samples (CZ-a and CZ, respectively) were compared for the oxidation of phenol (one-electron transfer reaction), the production of H_2 *via* water splitting and H_2O_2 production *via* oxygen reduction (both two-electron transfer reactions). Irrespective of the type of reaction, the CZ-a samples exhibit superior photocatalytic activities than the CZ samples in the following order: CZ-a-0.25 > CZ-a-0.5 > CZ-0.5 > CZ-0.25. The observed activity order is consistent with the trend observed in the XRD intensity ratio between the (100) and (002) planes (*i.e.*, I_{100}/I_{002} ratio) of the corresponding samples. The time-resolved photoluminescence decay spectra further reveal that the average lifetime of charge carriers is the shortest for CZ-a-0.25, followed by CZ-a-0.5, CZ-0.5 and CZ-0.25, which is consistent with the trends in the I_{100}/I_{002} ratio and the photocatalytic activity. The growth mechanism of the samples and the key factors determining the photocatalytic activity are discussed. Finally, the detailed surface characterization of the samples is described.

1.   Introduction

Semiconductor photocatalysis has been considered a core technology in the solar production of renewable chemical fuels *via* water splitting and CO_2 conversion,[1–4] as well as in the environmental remediation of contaminated air and water.[2,5] Knowledge on the fundamental aspects of photocatalysis has been gradually increasing, whereas practical applications are still limited owing primarily to the low photocatalytic efficiency and costly separation steps required when using semiconductor particles. Their low efficiency has been attributed to limited light absorption and sluggish charge transfer and injection,[4] which can be overcome by controlling the morphology, improving the crystallinity and modifying the semiconductor surface.[6] The latter challenge can be addressed by embedding a particulate semiconductor into a solid matrix (*e.g.*, polymeric membranes, well-defined porous oxides with large surface area and metal plates).[7–9]

There are a number of semiconductor photocatalysts such as TiO_2,[2,4,5] WO_3[10,11] and ZnO,[12–14] of which ZnO is unique in terms of ease of synthesis, facile morphology tailoring, and crystallinity- and morphology-specific reactivity. For example, ZnO rods have been reported to be active for single-electron transfer reactions including the decomposition of methylene blue and phenol, the production of OH radicals and the generation of photocurrents.[12] On the other hand, ZnO plates have been found more effective for the production of molecular hydrogen and hydrogen peroxide, both of which are initiated by two-electron transfer reactions. This morphology-specific reactivity is associated to oxygen vacancies and oxygen interstitials.[15]

In order to be suitable for a wide range of applications, ZnO needs to be embedded in a solid matrix, which not only avoids the post-separation step of the ZnO particles, but also promotes their photocatalytic activity. Successful embedding requires strong adherence between ZnO and the support, and the minimized loss of catalytic reactivity during the attachment

[a] Division of Nano & Energy Convergence Research, Daegu Gyeongbuk Institute of Science and Technology (DGIST), Daegu 42988, Republic of Korea. E-mail: limsk@dgist.ac.kr

[b] School of Energy Engineering, Kyungpook National University, Daegu 41566, Republic of Korea. E-mail: hwp@knu.ac.kr

† Electronic supplementary information (ESI) available. See DOI: 10.1039/c6ra15931a

process, while the support needs to possess a high specific surface area and an appropriate adsorption affinity towards the chemicals of interest.[16] A number of ZnO supports are available, including zeolites,[17] membranes[18] and porous carbon materials (such as activated carbon,[16,19] carbon nanotubes,[20–23] carbon nanofibers[14,22] and graphene[24]). Among these, carbon nanofiber (CNF) acts as a suitable platform to support ZnO owing to its chemical stability, large surface area and strong adherence towards ZnO.[25] In addition, CNF possesses high electrical conductivity (1.70×10^4 S m^{-1})[26] and catalytic activity, facilitating charge transfer and improving the charge injection efficiency (*i.e.*, the catalytic activity).

In this work, we synthesized ZnO rods rooted on manifold CNF paper *via* an electrodeposition process. The electrospun CNF was folded as manifold paper; then, ZnO was grown as polycrystalline and single crystalline rods with convex and concave-shaped ends, respectively. The as-fabricated CNF/ZnO samples were characterized using various surface analysis techniques and their photocatalytic activities were systematically evaluated in terms of an oxidation reaction (the decomposition of phenol) and two reduction reactions (the production of H_2 from water and H_2O_2 from O_2). In addition, efforts were made to examine the effect of the ZnO rod shape on the photocatalytic activity of CNF/ZnO and identify the primary factors influencing the activity.

2. Experimental

2.1. Preparation of CNF and CNF/ZnO

CNF webs were prepared following the electrospinning and carbonization procedure reported elsewhere.[27,28] In brief, a polyacrylonitrile (PAN, molecular weight 150 K, Aldrich) solution (10 wt%) was prepared by dissolving PAN in *N,N*-dimethylformamide (DMF, Sigma Aldrich) and heating at 60 °C under stirring for 4 h, followed by cooling it to room temperature while stirring for 12 h. The PAN solution was placed in a hypodermic syringe with a 25 gauge (0.2 mm) stainless steel nozzle, positioned at a fixed distance (~15 cm) from a metal cathode (collector). An electric field of 20 kV was applied between the nozzle and the collector. The electrospinning process produced PAN nanofibers on the collector plate. The collected PAN nanofibers were then annealed in three stages: (1) increasing the temperature at a ramping rate of 5 °C min^{-1} for 50 min and maintaining the end temperature (250 °C) for 20 min in air and for 10 min under a N$_2$ gas stream; (2) increasing the temperature to 750 °C at the same ramping rate and maintaining the temperature for 1 h under N$_2$ atmosphere; and (3) increasing the temperature to 1400 °C at the same ramping rate and maintaining the temperature for 1 h. The resulting ~65 μm-thick CNF film was folded five times to obtain a ~350 μm-thick film (see Fig. S1, ESI†).

For the synthesis of CNF/ZnO, the as-fabricated CNF films (1 cm × 3 cm, working electrode), an Ag/AgCl reference electrode and a Pt wire counter electrode were placed in two different aqueous solutions (50 mL) of zinc acetate (>99.9%, Aldrich) at concentrations of 0.25 and 0.5 mM. Then, each solution was heated to 60 °C at a ramping rate of 5 °C min^{-1} in a water bath.

After 30 min, the CNF films were biased at −1 V *vs.* Ag/AgCl for 30 min using a potentiostat (Bio Logic Science Instruments, VSP) and dried at 80 °C for 6 h (hereafter denoted as CZ). To improve the crystallinity of ZnO, the CNF/ZnO (CZ) samples were annealed at 400 °C for 30 min in air (denoted CZ-a). The amount of ZnO deposited on the CNF films was estimated by weighing the CNF films before and after the electrodeposition of ZnO.

2.2. Characterization

The morphology and elemental composition of the as-prepared samples were examined using high-resolution field emission scanning electron microscopy (FE-SEM, Hitachi, S-8020). The high-resolution morphological images and selected area electron diffraction (SAED) patterns were obtained with a transmission electron microscope (TEM, Hitachi, HF-3300, operating at 300 kV). X-ray diffraction (XRD) patterns were acquired with an X-ray diffractometer (Panalytical, Empyrean, 60 kV) using Cu-Kα_1 radiation ($\lambda = 1.54178$ Å) and a quartz monochromator. Diffused reflection spectroscopy (DRS) was performed using a UV-vis spectrometer (Shimadzu, UV 2450) in the wavelength range from 200 nm to 800 nm. The Brunauer–Emmett–Teller (BET) surface area of the samples was measured from nitrogen adsorption–desorption isotherms at 77 K (Micrometrics, ASAP 2020). The effective surface area was estimated at a relative pressure (P/P_0) ranging from 0.06 to 1.

The fluorescence lifetime decays were measured using an inverted-type scanning confocal microscope (Picoquant, MicroTime-200, Germany) with a 20× objective. A single-mode pulsed diode laser (379 nm with a pulse width of ∼200 ps and a laser power of ∼20 μW) was used as the excitation source. A dichroic mirror (AHF, Z375RDC), a long-pass filter (AHF, HQ405lp), a 50 μm pinhole, a band-pass filter and an avalanche photodiode detector (MPD, PDM series) were used to collect the emission from the ZnO/CNF sample. A time-correlated single-photon counting technique was used to obtain fluorescence decay curves as a function of time with a resolution of 16 ps during image scanning. Exponential fittings for the obtained fluorescence decays were performed *via* iterative least-squares deconvolution fitting using the Symphotime software (version 5.3).

2.3. Photocatalytic and photoelectrocatalytic activity tests

The as-fabricated samples (1 cm × 3 cm, 4.60 ± 0.23 mg) were vertically placed in a quartz reactor containing various aqueous media for redox reactions (oxidation reaction: phenol degradation and OH radical generation; reduction reactions: production of H_2 and H_2O_2) under UV light irradiation ($\lambda > 295$ nm) generated from a 300 W Xe-arc lamp (Newport). For the oxidation reaction of phenol, an air-equilibrated aqueous phenol solution (0.2 mM; 50 mL) was used. The concentration of phenol was intermittently determined using high-performance liquid chromatography (HPLC, YL instrument, YL 9100) following an analytical protocol reported elsewhere.[12] Irrespective of CNF/ZnO film samples, the adsorption of phenol was found to be insignificant (Table S1, ESI†). The photogenerated OH radicals were quantified using a colorimetric method using *N,N*-dimethyl-4-nitrosoaniline (RNO, Aldrich, 50 μM) as a quencher
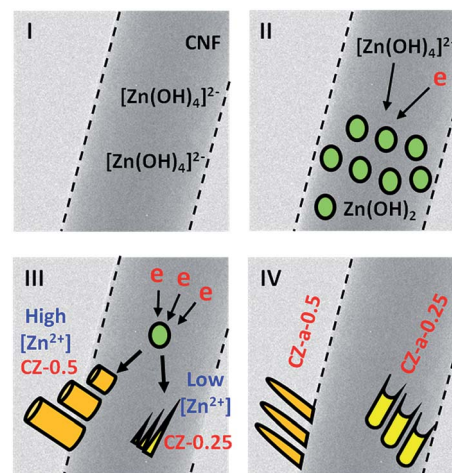
as reported elsewhere.[29] For the H$_2$ evolution reaction, the samples were immersed in a mixed aqueous solution of Na$_2$S (0.1 M) and Na$_2$SO$_3$ (0.1 M), and purged with N$_2$ for 1 h prior to irradiation. During the photoreaction, the headspace H$_2$ was intermittently quantified using gas chromatography (GC, Agilent, 6890N) equipped with a Porapak-Q column and a thermal conductivity detector (TCD). For the H$_2$O$_2$ production, the samples were immersed in an aqueous Na$_2$SO$_4$ solution (0.1 mM) and O$_2$ was purged through the solution during the reaction. H$_2$O$_2$ was intermittently quantified using a colorimetric method reported elsewhere.[30] The incident photon-to-current efficiency (IPCE) of the samples was estimated using a potentiostat/galvanostat (Princeton Applied Research, VersaSTAT 3). The as-synthesized samples (working electrode), Ag/AgCl reference electrode and Pt mesh counter electrode were immersed in an aqueous mixture of Na$_2$S (0.1 M) and Na$_2$SO$_3$ (0.1 M). The working electrode was held at −0.2 V vs. Ag/AgCl during irradiation with monochromated light from a CS 130 monochromator (Spectro Scientific, Mmac-200) with a 300 W Xe arc lamp. The IPCE values were estimated using the following equation: IPCE (%) = (1240 × I_{ph}) × 100/(P_{light} × λ), where I_{ph}, P_{light}, and λ refer to the photocurrent density at −0.2 V vs. Ag/AgCl, the photon flux and the wavelength, respectively. A detailed analytical procedure has been described elsewhere.[31,32]
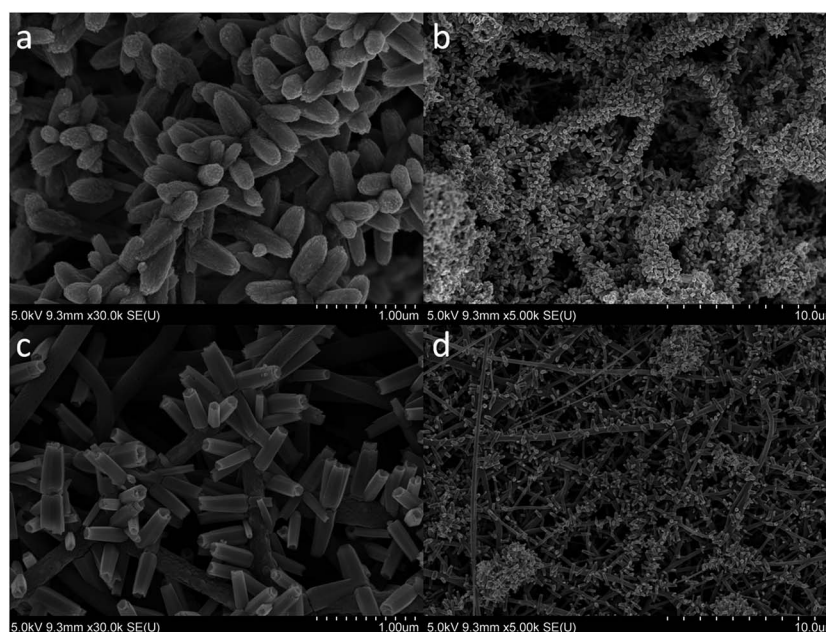
3. Results and discussion

3.1. Characterization of CNF/ZnO synthesized via electrodeposition

Fig. 1 shows the SEM images of the CNF/ZnO samples synthesized via electrodeposition of ZnO at [Zn^{2+}] = 0.5 and 0.25 mM,

followed by annealing at 400 °C for 30 min in air. In the electrodeposition process, the zinc precursor was hydrolyzed to Zn(OH)$_4$$^{2-}$ and further transformed to Zn(OH)$_2$ in the CNF held at E = −1 V vs. Ag/AgCl (Scheme 1). These zinc nuclei were then oxidized to ZnO while growing on the carbon fiber framework during oxidative annealing. The non-annealed CNF/ZnO sample prepared at [Zn^{2+}] = 0.5 mM (denoted CZ-0.5) presents a uniform distribution of a number of prism hexagonal shaped

Scheme 1 A schematic illustration of the formation of ZnO rods on CNF via electrodeposition and oxidative annealing. (I) Ionization of zinc acetate and the formation of [Zn(OH)$_4$]$^{2-}$ via water electrolysis. (II) ZnO nucleation on the CNF surface and formation of Zn(OH)$_2$ through electrodeposition followed by dehydration. (III) Formation of ZnO with different morphologies. (IV) ZnO growth on the CNF surface during annealing.

Fig. 1 SEM images of the (a and b) CZ-a-0.5 and (c and d) CZ-a-0.25 samples synthesized via the electrodeposition of ZnO on manifold carbon nanofiber paper placed in an aqueous solutions of zinc acetate at 0.5 and 0.25 mM, respectively followed by annealing at 400 °C for 30 min in air. The SEM images of the non-annealed samples (i.e., CZ-0.5 and CZ-0.25) are shown in Fig. S2.† See the Experimental section for the detailed fabrication process.

ZnO seeds with a size of ~400 nm on the fiber framework (Fig. S2a and b, ESI†). At low [Zn^{2+}] (0.25 mM, denoted CZ-0.25), irregular but needle-like ZnO seeds were formed with a size of ~180 nm (Fig. S2c and d, ESI†). The oxidative annealing step significantly changed the morphology of the samples. At high [Zn^{2+}], a number of ~530 nm-long ZnO rods with round, convex ends were grown and tightly packed on the CNF (denoted CZ-a-0.5, see Fig. 1a and b). At low [Zn^{2+}], on the other hand, ~540 nm-long ZnO rods with hexagonal shape, concave ends were formed (denoted CZ-a-0.25, Fig. 1c and d). The formation of ZnO rods on the CNF framework was further evidenced by mapping the Zn, O and C content (Fig. S3, ESI†). Different ZnO seed shapes were contemplated to strongly influence the morphology of the annealed samples. During the annealing process, although the vertical growth of ZnO was maintained regardless of the ZnO seed morphology, the ZnO needles appeared to be filling the inter space among the ZnO seeds on the CNF slower than the ZnO prisms. This appears to lead to ZnO rods with concave ends (Scheme 1).

Fig. 2 shows the TEM images and SAED patterns of the CZ-a-0.5 and CZ-a-0.25 samples. Although the overall length was quite similar, it is evident that CZ-a-0.5 and CZ-a-0.25 display

Fig. 2 (a and d) TEM morphology images, (b and e) lattice fringe spaces images and (c and f) SAED images of the (a–c) CZ-a-0.5 and (d–f) CZ-a-0.25 samples.
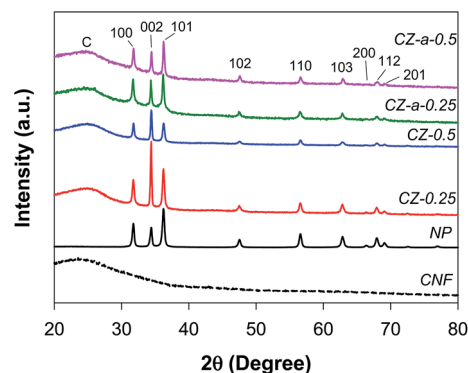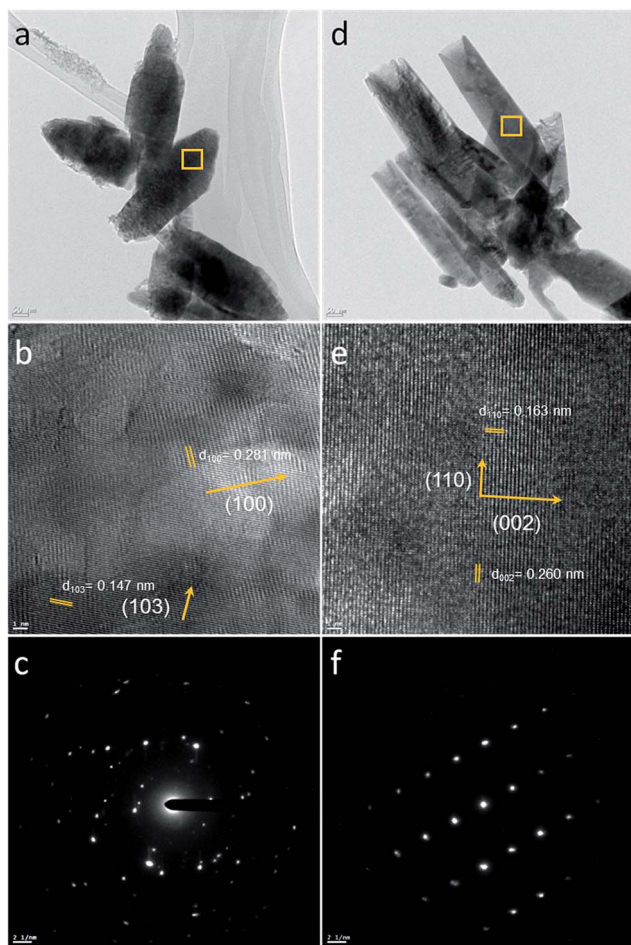

Fig. 3 XRD patterns of the samples. C refers to carbon (JCPDS #13-0148). The XRD pattern for ZnO indicates a hexagonal wurtzite structure (JCPDS #36-1451).

convex and concave ends, respectively. In addition, the high-resolution TEM images and SAED patterns indicate that CZ-a-0.5 and CZ-a-0.25 were composed of polycrystalline and single crystalline ZnO rods, respectively. The inter-plane spacing values of CZ-a-0.5, 0.281 and 0.147 nm, correspond to the (100) and (103) planes of ZnO, respectively. On the other hand, the observed inter-plane spacing values of CZ-a-0.25 (0.260 and 0.163 nm) were attributed to the (002) and (110) planes, respectively,[33] which indicates a preferential growth along the (0001) direction.

The crystalline structure of the CNF/ZnO samples was further examined by XRD (Fig. 3). All the ZnO-containing samples exhibited the same XRD pattern (e.g., $2\theta = 31.76°$, 34.421° and 36.252°, indexed to the (100), (002) and (101) planes, respectively), indicative of a hexagonal wurtzite structure (JCPDS #36-1451). The unit cell size of CZ-0.5 was smaller than that of commercial ZnO nanoparticles (NP, purchased from Aldrich), whereas the other samples showed a similar size (Table 1). CZ-a-0.5 and CZ-a-0.25 have similar c/a aspect ratios of 1.6021 and 1.6024, respectively, suggesting the anisotropic growth of ZnO. It is noteworthy that the intensity ratio of the (100) and (002) peaks (i.e., the I_{100}/I_{002} ratio) varied in the following order: CZ-a-0.25 (1.091) > CZ-a-0.5 (1.020) > CZ-0.5 (0.643) > CZ-0.25 (0.478) (Table 1). This ratio is known to be proportional to the photo-catalytic activity of ZnO since the (001) face is the most energetic among all faces.[13,34] Furthermore, this face is highly polar due to the preferential adsorption of hydroxide ions, leading to the

Table 1 The lattice constants and I_{100}/I_{002} ratios obtained for the samples

	CZ-a-0.25	CZ-a-0.5	CZ-0.25	CZ-0.5	NP
a (Å)	3.2490	3.2495	3.2498	3.2420	3.2501
c (Å)	5.2070	5.2069	5.2066	5.1760	5.2071
c/a	1.6024	1.6021	1.6026	1.5965	1.6021
V (Å³)^a	47.601	47.615	47.621	47.114	47.634
I_{100}/I_{002}	1.091	1.020	0.478	0.643	1.197

^{a} Unit cell volume (V) = ($\sqrt{3}/2$) × ($a^2 c$).

facile generation of OH radicals.[35] CZ-a-0.25 is thus expected to exhibit a higher photocatalytic activity than CZ-a-0.5, whereas CZ-0.5 could be superior to CZ-0.25 in this regard.

3.2. Photocatalytic activity of CNF/ZnO composites

The photocatalytic activity of the CNF/ZnO films was systematically evaluated for the degradation of phenol, and the productions of hydroxyl radical ($^{\bullet}$OH), H_2 and H_2O_2 under UV irradiation ($\lambda > 295$ nm) (Fig. 4). These photocatalytic reactions are well known and have been used as model reactions to examine the activity of new materials.[2,4] The phenol degradation proceeds primarily *via* oxidation by hydroxyl radicals that are generated through the one-electron oxidation of water (reactions 1 and 2; Fig. 4a). A similar trend of hydroxyl radical generation confirms this speculation (Fig. 4b). On the other hand, the latter two reactions proceed *via* the 2-electron reduction of protons and molecular oxygen, respectively (reactions 3 and 4; Fig. 4c and d).[12]

$$h^+ + H_2O \rightarrow {}^{\bullet}OH + H^+ \tag{1}$$

$$^{\bullet}OH + phenol \rightarrow degradation \tag{2}$$

$$2e^- + 2H^+ \rightarrow H_2 \tag{3}$$

$$2e^- + O_2 + 2H^+ \rightarrow H_2O_2 \tag{4}$$

Regardless of the type of reaction, the photocatalytic activity of the samples was found to be in the following order: CZ-a-0.25 > CZ-a-0.5 > CZ-0.5 > CZ-0.25 > NP (Fig. 4). When compared to the NP, the higher activity of the CZ samples was attributed to the combination of ZnO with CNF. In addition, the as-synthesized CZ samples were found to be highly durable (Fig. S4, ESI†). Carbon nanomaterials, including CNF, have been reported to enhance the photocatalytic activity of semiconductors,[36] particularly due to their high electrical conductivity, which facilitates charge transfer, as well as their catalytic properties towards charge injection.[37,38] The former was confirmed by impedance analysis (Fig. S5, ESI†), which clearly show that the charge transfer resistance (R_{ct}) of the CNF/ZnO samples is significantly lower than that of ZnO alone and further annealing decreases the R_{ct} value (Table S2, ESI†).[22,23,38]

There are several possible reasons for the observed order of photocatalytic activity for the CZ samples. First, the amount of ZnO loaded can be a primary factor. As shown in Fig. S6 (ESI†), an increase in the concentration of Zn^{2+} in the electrodeposition process leads to an increase in the amount of ZnO loaded on the CNF. For example, approximately 0.6 and 0.95 mg of ZnO were loaded on the CNF when a $[Zn^{2+}]$ of 0.25 and 0.5 mM were used in the electrodeposition process, respectively. These content values are below 10% of the CNF weight (~12.1 mg). A large amount of ZnO was beneficial for improving the photocatalytic activity, particularly when comparing the CZ-0.5 and CZ-0.25 samples. In contrast, CZ-a-0.25 exhibits a higher activity than CZ-a-0.5, which suggests that the amount of ZnO was not the sole factor determining the overall photocatalytic activity. Considering that photocatalysis is only initiated upon the
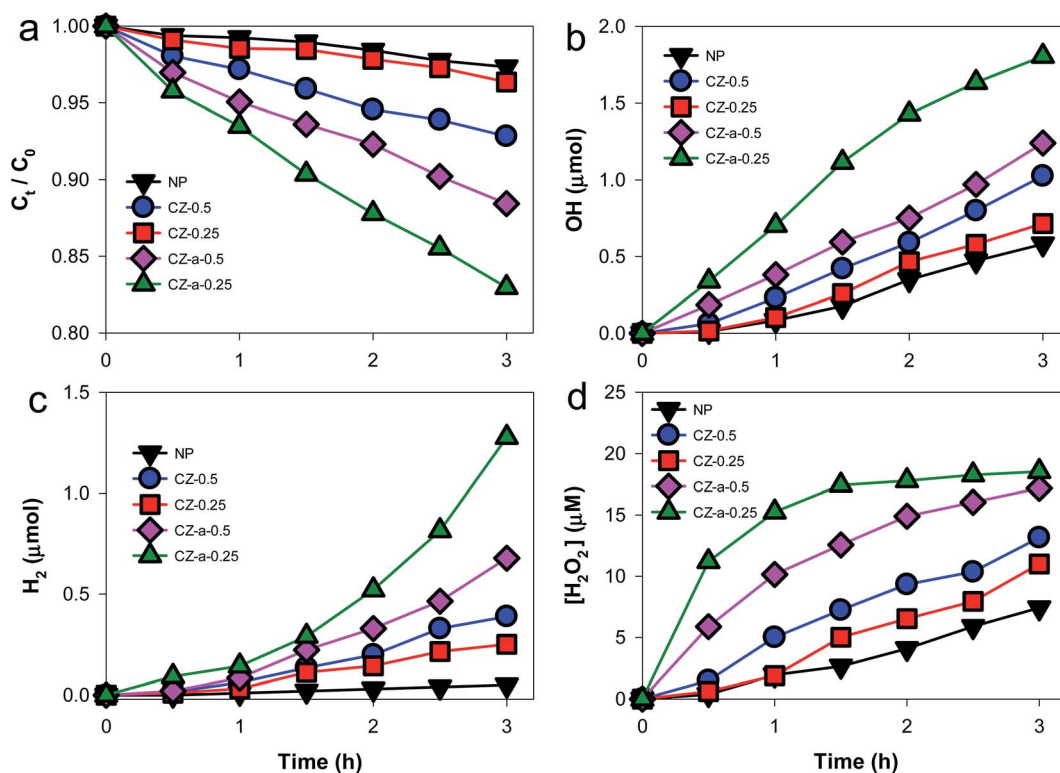

Fig. 4 The photocatalytic activity of the as-synthesized samples for (a) phenol (PhOH, 200 μM) degradation, (b) OH radical generation, (c) H_2 production in an aqueous sulfide/sulfite mixture (each 0.1 M) and (d) H_2O_2 production *via* O_2 reduction.

absorption of photons, the photocatalytic activity does not necessarily increase with a larger amount of semiconductor material, since there should be a portion of the particles not "hit" by the photons. The overall activity was determined by multiple factors including absorption, charge separation and catalysis, all of which are associated with the properties of the material, the type of reaction and the operating conditions.

Secondly, the as-synthesized samples possess similar UV-vis absorption spectra in terms of the absorption onset ($\sim$390 nm, corresponding to a bandgap of $\sim$3.18 eV, Fig. S7, ESI†). This suggests that the bandgap of ZnO is not significantly altered by either the concentration of Zn^{2+} or the presence of CNF. The absorption at $\lambda > 400$ nm is attributed to the black CNF and/or a scattering effect of the CZ samples. The BET surface area was also found to be quite similar among the samples at 9–12 m^2 g^{-1}, while the CNF itself showed a surface area of $\sim$10 m^2 g^{-1} (Fig. S8, ESI†). Accordingly, these properties should not influence the photocatalytic activity significantly.

Finally, we attempted to correlate the crystalline characteristics and the photocatalytic activity because the I_{100}/I_{002} ratio trend appeared to match that of the photocatalytic activity. For this purpose, the degradation rate constant of phenol (k_{PhOH}, where PhOH refers to phenol) was estimated by fitting the obtained data to the pseudo-first order kinetics equation (eqn (5)).

$$[PhOH]_t = [PhOH]_0 \exp(-k_{PhOH}t) \quad (5)$$

In addition, the rate constant of H_2O_2 production ($k_{H_2O_2}$) was obtained from the kinetic equations below (eqn (6) and (7)), as reported elsewhere.[39]

$$d[H_2O_2]/dt = (\Phi_0 - \Phi_1[H_2O_2])d[h\nu]_{abs}/dt \quad (6)$$

$$[H_2O_2]_t = \Phi_0/\Phi_1(1 - \exp(-k_{H_2O_2}t)) \quad (7)$$

where, Φ_0 and Φ_1 are the quantum yields for H_2O_2 formation and degradation, respectively, and d[$h\nu$]$_{abs}$/dt is the photon flux; $k_{H_2O_2}$ is a function of the photon flux and Φ_1 (*i.e.*, d[$h\nu$]$_{abs}$/dt $\times$ Φ_1). As for the H_2 production, only the linear regions of production (*i.e.*, between 2 and 3 h) were considered (Fig. 4c)

because there is usually an induction period in the early stages of film-type photocatalysis.[28,40,41] These rate constants (k_{PhOH}, $k_{H_2O_2}$, and k_{H_2}) were re-plotted with respect to the I_{100}/I_{002} ratio (Fig. 5). It is evident that a certain correlation exists among the CZ samples, with the exception of CZ-a-0.25. This suggests that deposition on CNF leads to an enhancement in the photocatalytic activity, while an increase in the I_{100}/I_{002} ratio can maximize the activity. While the latter concerns a property of ZnO and is rather difficult to control, the former can be easily achieved without significant effort.

3.3. Ultrafast charge transfer in CNF/ZnO

The charge transfer kinetics of the as-synthesized CZ samples were characterized *via* time-resolved photoluminescence (TRP) decay analysis (Fig. 6a). Upon excitation at $\lambda = 379$ nm, the emission decayed exponentially and the decay constants were estimated by fitting the decay curves to the following equation: $I(t) = A_1 \exp(-t/\tau_1) + A_2 \exp(-t/\tau_2) + A_3 \exp(-t/\tau_3)$, where $I(t)$ is the time-dependent photoluminescence intensity, A is the normalized amplitude of the corresponding lifetime

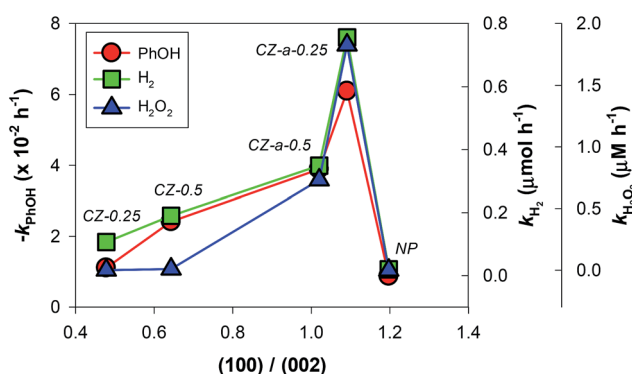|	CZ-0.5	CZ-0.25	CZ-a-0.5	CZ-a-0.25	NP
A1	28.7	24.8	32.8	23.7	31.5
t1 / ns	7.33	6.68	4.75	7.08	17.19
A2	59.1	66.7	58.0	68.5	68.5
t2 / ns	1.02	0.81	0.49	0.89	2419.84
A3	12.2	8.5	9.2	7.7	
t3 / ns	60.30	61.53	59.20	63.01	
Ave. t / ns	10.08	7.46	7.26	7.17	1662.45

Fig. 5 Plots for the XRD peak intensity ratio of the (100) and (002) planes (I_{100}/I_{002}) vs. the observed rate constants for phenol (PhOH) degradation (red circles), H_2 production (green rectangles) and H_2O_2 production (blue triangles).
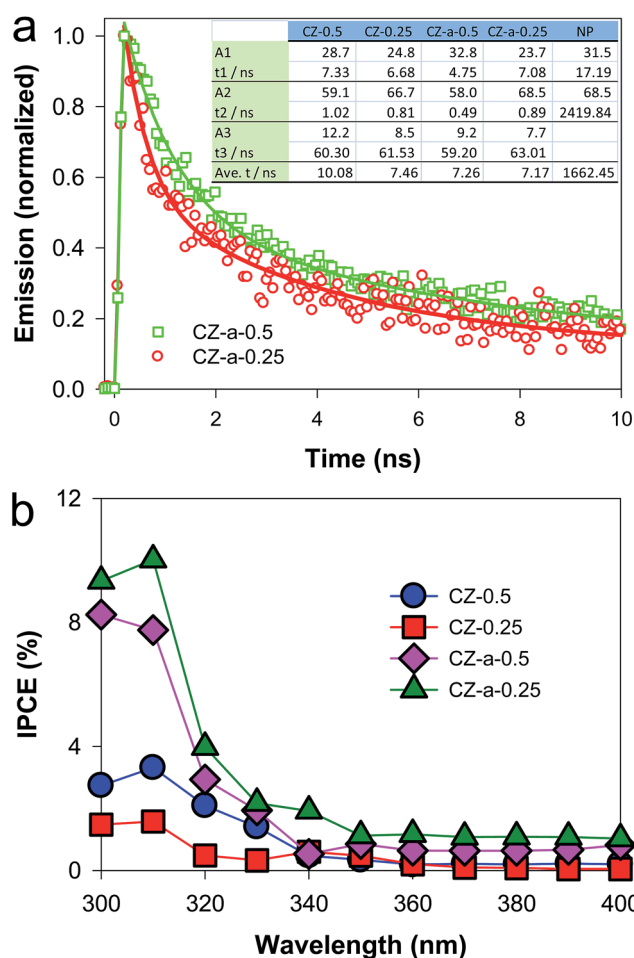
Fig. 6 (a) The fluorescence lifetime decay curves obtained for CZ-a-0.5 and CZ-a-0.25. The inset shows the lifetimes of the charge carriers in the samples. See text for more information. (b) IPCE values obtained for the samples with respect to the wavelength.

component and τ is the photoluminescence lifetime.[42] Two primary phenomena were found in the TRP decay spectra. First, each CZ sample has three lifetimes, whereas the NP sample presents only two lifetimes. This reveals that the charge transfer pathways in ZnO change upon deposition on the CNF. Secondly, the average lifetime of CZ-a-0.25 (7.17 ns) is the shortest, followed by those of CZ-a-0.5 (7.26 ns), CZ-0.5 (7.46 ns), and CZ-0.25 (10.08 ns). Surprisingly, this trend is the same as those of the I_{100}/I_{002} ratio and the photocatalytic activity. Although the lifetimes were similar at 7–10 ns, they were two orders of magnitude shorter than those found for the NP (1662 ns).

Ultrafast charge transfer should lead to an increase in the photocurrent. To examine this speculation, the incident photon-to-current efficiency (IPCE) of the as-synthesized CZ samples was measured upon applying a potential of −0.2 V *vs.* Ag/AgCl while shining light on the samples. As shown in Fig. 6b, the IPCE of CZ-a-0.25 at $\lambda = 310$ nm was ∼10% and decreased substantially to ∼1% in the range of 380–400 nm. This IPCE profile with respect to the wavelength was similar to the absorption spectrum of CZ-a-0.25 (Fig. S7, ESI†). CZ-a-0.5 exhibits a similar profile, whereas the non-annealed samples show significantly smaller IPCE values even in the short wavelength regions. It is noteworthy that the IPCE value order is the same as the photocatalytic activity order.

4. Conclusions

Crystalline ZnO rods were successfully grown in manifold carbon nanofiber paper by electrodeposition and the morphology of the ZnO rods was tailored by changing the zinc precursor concentration. At a relatively high concentration of the zinc precursor, polycrystalline ZnO rods with convex-shaped ends were predominantly grown, whereas single crystalline ZnO rods with concave ends were synthesized at a lower ZnO concentration. Although the deposited amount of ZnO was smaller, the latter exhibited superior photocatalytic activity for the oxidative decomposition of phenol as well as for the reductive formation of H_2 and H_2O_2. Considering that phenol decomposition proceeds predominantly by OH radicals generated by one-electron oxidation of water and that H_2 and H_2O_2 are produced *via* two-electron transfer reductions of the respective water and O_2, the composites comprised of single crystalline ZnO rods and CNF paper possess superior photocatalytic properties for single and multiple charge transfer and injection processes. The primary factor determining these properties appears to be the XRD intensity ratio of the (100) and (002) planes (*i.e.*, I_{100}/I_{002} ratio) of the composites. The time-resolved photoluminescence decay spectra and IPCE profiles of the samples support this hypothesis. The presented synthetic process provides several potential advantages, which include the facile synthesis and tailoring of the thickness and size of the CNF paper, as well as the facile yet well-controlled growth of crystalline ZnO rods.

Acknowledgements

References

1 H.-J. Lewerenz and L. Peter, *Photoelectrochemical Water Splitting: Materials, Processes and Architectures*, RSC Publishing, Cambridge, 1st edn, 2013.

2 H. Park, Y. Park, W. Kim and W. Choi, *J. Photochem. Photobiol., C*, 2013, **15**, 1–20.

3 J. S. Jang and H. Park, in *Materials and Processes for Solar Fuel Production*, ed. B. Viswanathan, V. Subramanian and J. S. Lee, Springer, Berlin, 1st edn, 2014, pp. 1–22.

4 H. Park, H. I. Kim, G. H. Moon and W. Choi, *Energy Environ. Sci.*, 2016, **9**, 411–433.

5 M. R. Hoffmann, S. T. Martin, W. Y. Choi and D. W. Bahnemann, *Chem. Rev.*, 1995, **95**, 69–96.

6 H. W. Jeong, T. H. Jeon, J. S. Jang, W. Choi and H. Park, *J. Phys. Chem. C*, 2013, **117**, 9104–9112.

7 M. D'Arienzo, M. Crippa, A. A. Essawy, R. Scotti, L. Wahba, F. Morazzoni, P. Gentile, I. R. Bellobono and S. Polizzi, *J. Phys. Chem. C*, 2010, **114**, 15755–15762.

8 L. Zhang, Y. F. Zhu, Y. He, W. Li and H. B. Sun, *Appl. Catal., B*, 2003, **40**, 287–292.

9 L. L. Feng, X. Zou, J. Zhao, L. J. Zhou, D. J. Wang, X. Zhang and G. D. Li, *Chem. Commun.*, 2013, **49**, 9788–9790.

10 N. C. Deb Nath, S. Y. Choi, H. W. Jeong, J.-J. Lee and H. Park, *Nano Energy*, 2016, **25**, 51–59.

11 H. Park, A. Bak, T. H. Jeon, S. Kim and W. Choi, *Appl. Catal., B*, 2012, **115**, 74–80.

12 H. W. Jeong, S. Y. Choi, S. H. Hong, S. K. Lim, D. S. Han, A. Abdel-Wahab and H. Park, *J. Phys. Chem. C*, 2014, **118**, 21331–21338.

13 A. McLaren, T. Valdes-Solis, G. Li and S. C. Tsang, *J. Am. Chem. Soc.*, 2009, **131**, 12540–12541.

14 J. Mu, C. Shao, Z. Guo, Z. Zhang, M. Zhang, P. Zhang, B. Chen and Y. Liu, *ACS Appl. Mater. Interfaces*, 2011, **3**, 590–596.

15 L. Schmidt-Mende and J. L. MacManus-Driscoll, *Mater. Today*, 2007, **10**, 40–48.

16 A. Y. Shan, T. I. M. Ghazi and S. A. Rashid, *Appl. Catal., A*, 2010, **389**, 1–8.

17 Q. J. Yu, C. Y. Li, X. L. Tang and H. H. Yi, *RSC Adv.*, 2015, **5**, 8152–8162.

18 J. Wang, P. Liu, X. Fu, Z. Li, W. Han and X. Wang, *Langmuir*, 2009, **25**, 1218–1223.

19 S. H. Hwang, H. J. Seo, Y. K. Kim and S. K. Lim, *Mater. Sci. Semicond. Process.*, 2016, **41**, 226–232.

20 W. D. Zhang, L. C. Jiang and J. S. Ye, *J. Phys. Chem. C*, 2009, **113**, 16247–16253.

21 Y. K. Kim, G. Khan, H. W. Jeong and H. Park, *Rapid Communication in Photoscience*, 2014, **3**, 56–58.

22 G. Khan, Y. K. Kim, S. K. Choi, D. S. Han, A. Abdel-Wahab and H. Park, *Bull. Korean Chem. Soc.*, 2013, **34**, 1137–1144.

23 Y. K. Kim and H. Park, *Energy Environ. Sci.*, 2011, **4**, 685–694.

24 X. J. Men, H. B. Chen, K. W. Chang, X. F. Fang, C. F. Wu, W. P. Qin and S. Y. Yin, *Appl. Catal., B*, 2016, **187**, 367–374.

25 J. S. Bonso, G. D. Kalaw and J. P. Ferraris, *J. Mater. Chem. A*, 2014, **2**, 418–424.

26 C. S. Sharma, H. Katepalli, A. Sharma and M. Madou, *Carbon*, 2011, **49**, 1727–1732.

27 S. Kim and S. K. Lim, *Appl. Catal., B*, 2008, **84**, 16–20.

28 Y. K. Kim, M. Kim, S. H. Hwang, S. K. Lim, H. Park and S. Kim, *Int. J. Hydrogen Energy*, 2015, **40**, 136–145.

29 S. Y. Yang, W. Choi and H. Park, *ACS Appl. Mater. Interfaces*, 2015, **7**, 1907–1914.

30 K. Kosaka, H. Yamada, S. Matsui, S. Echigo and K. Shishida, *Environ. Sci. Technol.*, 1998, **32**, 3821–3824.

31 U. Kang, S. K. Choi, D. J. Ham, S. M. Ji, W. Choi, D. S. Han, A. Abdel-Wahab and H. Park, *Energy Environ. Sci.*, 2015, **8**, 2638–2643.

32 U. Kang and H. Park, *Appl. Catal., B*, 2013, **140**, 233–240.

33 H. Wang, M. Li, L. Jia, L. Li, G. Wang, Y. Zhang and G. Li, *Nanoscale Res. Lett.*, 2010, **5**, 1102–1106.

34 M. L. Huang, Y. Yan, W. H. Feng, S. X. Weng, Z. Y. Zheng, X. Z. Fu and P. Liu, *Cryst. Growth Des.*, 2014, **14**, 2179–2186.

35 A. Dodd, A. McKinley, T. Tsuzuki and M. Saunders, *Mater. Chem. Phys.*, 2009, **114**, 382–386.

36 S. Fang, Y. Xia, K. L. Lv, Q. Li, J. Sun and M. Li, *Appl. Catal., B*, 2016, **185**, 225–232.

37 Y. K. Kim and H. Park, *Appl. Catal., B*, 2012, **125**, 530–537.

38 H. W. Jeong and H. Park, *Catal. Today*, 2014, **230**, 15–19.

39 C. Kormann, D. W. Bahnemann and M. R. Hoffmann, *Environ. Sci. Technol.*, 1988, **22**, 798–806.

40 H. Park, Y. Park, E. Bae and W. Choi, *J. Photochem. Photobiol., A*, 2009, **203**, 112–118.

41 Y. K. Kim, S. K. Lim, H. Park, M. R. Hoffmann and S. Kim, *Appl. Catal., B*, 2016, **196**, 216–222.

42 A. Pal, S. Srivastava, R. Gupta and S. Sapra, *Phys. Chem. Chem. Phys.*, 2013, **15**, 15888–15895.